Paramagnetism-Based Refinement Strategy for the Solution Structure of Human α-Parvalbumin †

7 AUTHORS, INCLUDING:

Yogesh K Gupta
Icahn School of Medicine at Mount Sinai
18 PUBLICATIONS **261** CITATIONS

SEE PROFILE

Yong-Min Lee
Ewha Womans University
142 PUBLICATIONS **3,583** CITATIONS

SEE PROFILE

Claudio Luchinat
University of Florence
614 PUBLICATIONS **14,682** CITATIONS

SEE PROFILE

Alessandro Quattrone
Università degli Studi di Trento
110 PUBLICATIONS **2,300** CITATIONS

SEE PROFILE

Article

Paramagnetism-Based Refinement Strategy for the Solution Structure of Human □-Parvalbumin

Irfan Baig, Ivano Bertini, Cristina Del Bianco, Yogesh Kumar Gupta, Yong-Min Lee, Claudio Luchinat, and Alessandro Quattrone

More About This Article

Additional resources and features associated with this article are available within the HTML version:

- Supporting Information
- Access to high resolution figures
- Links to articles and content related to this article
- Copyright permission to reproduce figures and/or text from this article

View the Full Text HTML

Paramagnetism-Based Refinement Strategy for the Solution Structure of Human α-Parvalbumin[†]

Irfan Baig,[‡] Ivano Bertini,*,[‡] Cristina Del Bianco,[‡] Yogesh Kumar Gupta,[‡] Yong-Min Lee,[‡] Claudio Luchinat,[§] and Alessandro Quattrone[||]

Magnetic Resonance Centre and Department of Chemistry, University of Florence, Via Luigi Sacconi 6, 50019 Sesto Fiorentino, Italy, Magnetic Resonance Centre and Department of Agricultural Biotechnology, P. le delle Cascine 28, 50144 Florence, Italy, and Medical Genetics Unit, IRCCS CSS, Viale Padre Pio, 71013 San Giovanni Rotondo (FG), Italy

ABSTRACT: In the frame of a research aimed at the detailed structural characterization of human calcium-binding proteins of the EF-hand family, the solution structure of human α-parvalbumin has been solved by NMR and refined with the help of substitution of the Ca^{2+} ion in the EF site with the paramagnetic Dy^{3+} ion. A simple $^1H-^{15}N$ HSQC spectrum allowed the NH assignments based on the properties of Dy^{3+}. This allowed us to exploit pseudocontact shifts and residual dipolar couplings for solution structure refinement. The backbone and heavy atom RMSD are 0.55 ± 0.08 and 1.02 ± 0.08 Å, respectively, and decrease to 0.39 ± 0.05 and 0.90 ± 0.06 Å upon refinement with paramagnetism-based restraints. The RMSD for the metal itself in the EF site in the refined structure is 0.26 ± 0.12 Å. Backbone NH R_1, R_2, and NOE measured at two temperatures show the protein to be relatively rigid. The NH orientations are well determined by the paramagnetism-based restraints. This allows us to detect small but significant local structural differences with the orthologue protein from rat, whose X-ray structure is available at 2.0 Å resolution. All differences are related to local changes in the amino acidic composition.

Ca^{2+} is a versatile intracellular messenger regulating a broad range of biochemical processes mainly through fluctuations in its cytosolic concentration. Ca^{2+} transients are dependent on the activity of either Ca^{2+}-gating systems, which regulate cytosolic Ca^{2+} trafficking from the extracellular space or from intracellular Ca^{2+} stores (mitochondria and endoplasmic reticulum cisternae), or Ca^{2+}-buffering systems, which are thought to modify the spatial and temporal dynamics of Ca^{2+} transients. Concerted action of these two systems shapes Ca^{2+} signals of very different types, ranging from rapid highly localized Ca^{2+} spikes, which regulate fast responses, to repetitive global Ca^{2+} waves, controlling mainly slower responses (*1*). The overall organization, the relative importance, and the specific function of the proteins belonging to the Ca^{2+}-buffering system are still a scientific challenge. The data available come primarily from a group of proteins belonging to the superfamily of the EF-hand-containing proteins, which includes α- and β-parvalbumin, calretinin, and calbindin D_{28k}. Among the

other superfamily members, these proteins are distinguished for selectivity of expression in tissues, specificity of distribution in cell subpopulations, high abundance, and the absence of a demonstrated Ca^{2+}-mediated triggering role on downstream cascades (*2*). The last observation is at the root of the hypothesis of their functional role as cytosolic Ca^{2+} buffers. Even though the biochemical and structural characterization of these proteins started more than 3 decades ago, very recently they have raised a new surge of interest mainly for the identification of critical roles in neuronal development and physiology (*3*, *4*).

In the frame of an effort to better define the structural determinants of biological activity for Ca^{2+}-buffering proteins, we have undertaken the solution structure of the protein products of two closely related human genes conserved in all vertebrate species, α-parvalbumin (PV)[1] and β-parvalbumin, also known as oncomodulin (OM) (*5*). Parvalbumins are low-molecular-mass (ca. 12 kDa), high-affinity Ca^{2+}-binding proteins containing three domains named AB, CD, and EF sites. They are characterized by a helix−loop−helix

---

* To whom correspondence should be addressed. Tel: +39055 4574272. Fax: +39055 4574271. E-mail: ivanobertini@cerm.unifi.it.
[‡] Magnetic Resonance Centre and Department of Chemistry, University of Florence.
[§] Magnetic Resonance Centre and Department of Agricultural Biotechnology.
[||] Medical Genetics Unit, IRCCS CSS.

[1] Abbreviations: PV, α-parvalbumin; OM, oncomodulin (β-parvalbumin); NMR, nuclear magnetic resonance; LB, Luria−Bertani; IPTG, isopropyl β-D-thiogalactopyranoside; Ni-NTA, nickel nitrilotriacetic acid; GABA, γ-aminobutyric acid; HSQC, heteronuclear single-quantum coherence; PCS, pseudocontact shifts; RDC, residual dipolar couplings; IPAP, in-phase/antiphase; TAD, torsion angle dynamics; REM, restrained energy minimization; CaCaPV, dicalcium parvalbumin; CaDyPV, Dy^{3+}-substituted parvalbumin; CBCANH, Cβ−Cα−NH connectivity experiment; CBCACONH, Cβ−Cα−carbonyl carbon−NH connectivity experiment; NOESY, nuclear Overhauser effect spectroscopy; TOCSY, total correlation spectroscopy; TROSY, transverse relaxation optimized spectroscopy; CSI, chemical shift index; CSA, chemical shift anisotropy.

motif. In the CD and EF sites the loop has the ability to bind Ca^{2+} ions. Motifs with this ability are commonly termed EF hands. In both PV and OM, the AB site is unable to bind Ca^{2+} due to the absence of an oxygen-bearing residue at the critical position in the central loop (*6*). The CD and EF sites are paired to form a stable structural domain and have a Ca^{2+}-binding affinity in the high range of that of other EF-hand-containing Ca^{2+}-binding proteins, as expected for buffering activity.

Functionally, from the analysis of knockout mice, a role for PV has been suggested in acceleration of the contraction–relaxation cycle of fast twitch muscle fibers (*7*) and in the generation of synchronous spikes in a network of GABAergic neurons in the cerebral cortex (*8, 9*).

A substantial amount of information on the structure of various vertebrate PV and OM has been obtained by X-ray crystallography and NMR spectroscopy (*5, 10–13*). However, structural information on the human proteins is still lacking. Although the high sequence identity between, for instance, rat and human orthologue parvalbumins is as high as 87%, past experience suggests that even small structural changes may be significant from the functional point of view in Ca^{2+}-binding proteins. As an example, calmodulin, the prototype Ca^{2+}-binding protein responsible for decoding Ca^{2+}-elicited signals in cells, is 100% identical in all of its vertebrate orthologues, and the protein from molluscs, differing by only three amino acids from the vertebrate one, has distinctively different Ca^{2+}-binding properties (*14*).

Here we present the solution structure and dynamics of human PV. According to a procedure which is pursued in our laboratory, the structure has been substantially refined with the help of paramagnetic lanthanide substitution for one of the Ca^{2+} sites, which provides additional and useful restraints, and a detailed structural insight is obtained.

MATERIALS AND METHODS

Plasmids, Bacterial Strains, Media, and Buffers. Escherichia coli XL1-Blue supercompetent cells (Stratagene) were used as the host strain for cloning and protein expression from the vector pQE-30 Xa (Qiagen). The transformed cells were routinely grown in Luria–Bertani (LB) broth or on plates of LB agar, supplemented with ampicillin (100 μg/mL). Induction was carried out both in rich LB broth and in M9 medium supplemented with 1 mM $CaCl_2$, 5 mM $MgSO_4$, 0.01% thiamin (w/v), and 3 g/L $^{15}NH_4(SO_4)_2$ and 4 g/L $[^{13}C_6]$-D-glucose (Cambridge Isotope Laboratory) as ^{15}N and ^{13}C sources. The following buffer composition was used: lysis buffer (50 mM sodium phosphate, pH 8.0, 300 mM NaCl, 10 mM imidazole, 1 mM PMSF).

Cloning, Expression, and Purification of Human α-Parvalbumin. The coding sequence for the full-length human α-parvalbumin was amplified from a human cerebellum cDNA library by PCR using the following forward, 5′-ATGTCGATGACAGACTTG-3′, and reverse, 5′-TTTAG-CTTTCAGCCACCAT-3′, primers. Native *Pfu* (Stratagene) was the polymerase used for amplification. The PCR product was gel purified and end-phosphorylated with T4 polynucle-otide kinase (Amersham). The pQE-30 Xa vector, able to express N-terminal His-tagged proteins, was used for cloning, after blunt-end linearization with the *Stu*I restriction enzyme and dephosphorylation with alkaline phosphatase (Strat-

agene). Positive bacterial clones were checked for the sequence of the cloned construct, and one was chosen for growth in 1 L of minimal medium containing $[^{15}N]$ammonium sulfate and $[^{13}C]$glucose at 37 °C, until reaching an A_{600} of 0.6. At this stage, the transformed culture was induced with 1 mM isopropyl β-D-thiogalactopyranoside (IPTG) followed by the continued incubation of the cultures for 14 h at 37 °C. Cells were then pelleted by centrifugation at 6000 rpm for 30 min and resuspended in 25 mL of ice-cold lysis buffer. Cell lysis was performed first by freezing–thawing (−70/37 °C) followed by sonication for 6 times × 20 s with a cooling period of 20 s between each burst. Lysate was centrifuged at 10000 rpm and the supernatant collected and subjected to purification. The His-tagged recombinant protein was purified by using Ni-NTA affinity chromatography (Qiagen) and used as such for NMR structure determination. A small amount of His-tag-lacking protein was also prepared and checked by NMR.

NMR Sample Preparation and Measurements. NMR samples were prepared by dissolving the protein in 550 μL of the solution containing 100 mM NaCl and 10% D_2O. The final concentrations of the ^{15}N- and $^{13}C/^{15}N$-labeled samples were 0.6 and 1.5 mM, respectively. The pH was adjusted to 7.0 by means of 0.01 M NaOH or 0.01 M HCl.

The NMR spectra were acquired on Bruker AVANCE 700, AVANCE 600, and DRX 500 spectrometers operating at proton nominal frequencies of 700.13, 600.13, and 500.13 MHz, respectively. All spectrometers are equipped with a triple-resonance (TXI) 5 mm probe with a *z*-axis pulse field gradient, and the 500 MHz spectrometer is equipped with a triple-resonance cryoprobe. All NMR experiments were performed at 298 K. All spectra were processed with the Bruker XWINNMR software packages and analyzed by the program XEASY (ETH Zürich) (*15*). The residual water signal was suppressed either by presaturation during both the relaxation delay and mixing time or by gradient-tailored excitation (WATERGATE) (*16*). The spectra were calibrated at different temperatures according to the empirical relationship (*17*) $\delta_{HOD} = (-0.012T + 5.11)$ ppm, with T being the temperature in degrees Celsius. All NMR experiments performed in this work are listed in the Supporting Information (Table S1). The samples were kept at 4 °C between measurements.

For the PCS values of the Dy^{3+}-substituted derivative, the $^1H-^{15}N$ HSQC (*18*) spectrum was recorded at 298 K using a spectral width of 14 and 38 ppm in the ^1H and ^{15}N dimensions, respectively. A total of 256 increments, each with 1024 complex data points and 48 transients, were collected. Raw data were multiplied in both dimensions by a squared cosine window function and Fourier transformed to obtain a final matrix of 1024 × 1024 or of 512 × 512 real data points for HSQC spectra. A polynomial baseline correction was applied in the f_2 dimension.

One-bond $^1H-^{15}N$ coupling constants were measured at 298 K and 700 MHz either by fitting a series of $^1J_{NH}$-modulated HSQC spectra (*19*) or by using the IPAP method (*20*).

All of the NMR experiments for measuring ^{15}N relaxation rates were performed at 283 and 298 K on a Bruker Avance 600 MHz spectrometer with a ^{15}N-enriched sample lacking the His tag. ^{15}N longitudinal relaxation rates, R_1, and ^{15}N transverse relaxation rates, R_2, were determined by collecting

a series of ^{1}H$-$^{15}N HSQC spectra with flip-back (*21*) and phase-sensitive pulse sequences (*22*−*24*). R_1 and R_2 were both measured with 10 different delays, and a CPMG pulse sequence (*23*) with a refocusing delay, τ_m, of 450 μs was used for the R_2 measurements. R_1 and R_2 were calculated by fitting cross-peak intensities as a function of the delay time to a single exponential decay using the Levenburg−Marquardt algorithm (*25*, *26*). Uncertainties were determined by using the Monte Carlo approach (*27*). Heteronuclear ^{1}H$-$^{15}N NOEs were measured by taking the ratio of peak volumes acquired with and without ^{1}H saturation.

Structure Calculation. ^{15}N and ^{13}C 3D NOESY-HSQC cross-peak intensities were integrated using the elliptical integration routine implemented in XEASY and converted into interatomic upper distance limits by the program CALIBA (*28*). Backbone dihedral ϕ and ψ angles, hydrogen bonds, and stereospecific assignments of diastereotopic protons were also used as diamagnetic constraints in the calculation with the standard DYANA parameters (*29*).

The program DYANA (*29*, *30*) employing torsion angle dynamics (TAD) combined with a simulated annealing algorithm was used to calculate a family of 200 structures starting from randomly generated conformers in 10000 annealing steps. The quality of structures calculated by DYANA can be assessed by a properly defined function (target function) proportional to the squared deviations of the calculated restraints from the experimental ones, plus the squared van der Waals contact violations. The Ca^{2+} in the N-terminal site and either the Ca^{2+} or the Dy^{3+} ion in the C-terminal site were added at the end of the sequence through a linker of pseudoatoms. The metal ions were imposed to be between 2.0 (lower limit) and 2.8 (upper limit) Å from the donor atoms, forming the EF-hand consensus sequence of donors (*31*−*33*).

The PCS and RDC values for the Dy^{3+}-substituted derivative were used as paramagnetic restraints, together with all diamagnetic restraints through the appropriate PARA-MAGNETIC-DYANA modules (*30*). A fixed tolerance of 0.10 ppm for the PCS values and 0.50 Hz for RDC values was used for the structural calculation. A fixed weight of 0.5 for the PCS values and 0.1 for RDC values was also used in the structural calculation. The 20 structures with the lowest target functions were included in the final families, and RMSD values from the mean for the backbone and all heavy atoms (which include carbon, nitrogen, oxygen, and sulfur atoms from the side chains) were calculated. The programs MOLMOL (*34*) and PROCHECK (*35*) were subsequently used for secondary structure analysis. The final family of 20 conformers was minimized by iterative cycles of PARAMAGNETIC-DYANA (*30*), followed by restrained energy minimization (REM) with AMBER 5.0 (*36*). For comparison purposes, a model structure of human parvalbumin was also built by the program MODELLER-4 (*37*) using as template the X-ray structure of rat parvalbumin (*38*).

The PDB coordinates and chemical shifts have been deposited in the Protein Data Bank and BMRB, respectively. (PDB codes 1RK9 and 1RJV and BMRB deposition no. BMRB-9704).

RESULTS

The 700 MHz ^{1}H$-$^{15}N and ^{1}H$-$^{13}C HSQC spectra (*18*) of human parvalbumin show that the protein is properly
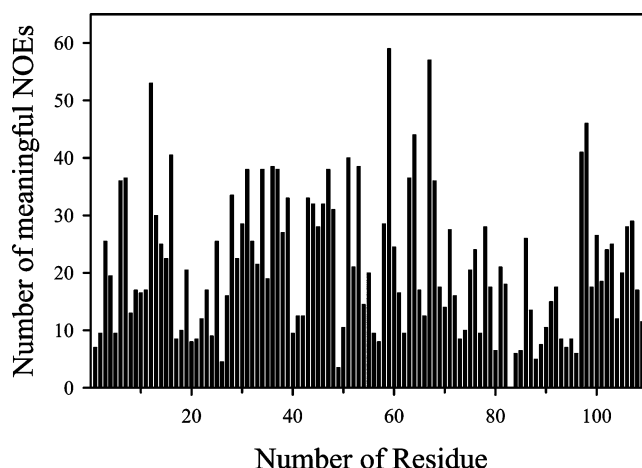

FIGURE 1: Plot of the number of meaningful NOEs per residue.

folded. The backbone resonance assignment was obtained by the analysis of CBCANH (*39*) and CBCA(CO)NH (*40*) spectra at 700 MHz; 108 out of 109 NH backbone amide resonances (excluding one proline) were assigned from these spectra. The missing one (His 49) was later found by analysis of the 700 MHz 3D NOESY-HSQC spectra. The resonances from the additional His tag at the N-terminus were not assigned. The assignment of the aliphatic side-chain reso-nances was performed through the analysis of 3D CC(CO)-NH (*41*) and (H)CCH-TOCSY (*42*) spectra at 700 MHz, together with 3D ^{15}N- and ^{13}C-NOESY-HSQC spectra, both performed at 700 MHz (*43*). The assignment of the aromatic spin systems was performed with 2D NOESY (*44*) and 2D TOCSY (*44*) maps at 700 MHz. $^3J_{HNH\alpha}$ coupling constants were determined through the 600 MHz HNHA (*45*) experi-ment. Good agreement of $^3J_{HNH\alpha}$ and NOE intensity ratios with CSI (*46*) estimates was found. Backbone dihedral ϕ angles were independently derived from $^3J_{HNH\alpha}$ coupling constants through the appropriate Karplus equation (*47*). Backbone dihedral ψ angles for residue $i - 1$ were also determined from the ratio of the intensities of the $d_{\alpha N}(i-1,i)$ and $d_{N\alpha}(i,i)$ NOEs present on the ^{15}N(i) plane of residue i obtained from the ^{15}N-edited NOESY-HSQC spectrum. Sixteen hydrogen bonds were detected from the analysis of the 500 MHz TROSY-like HNCO (*48*) experiment. The ^{1}H, ^{13}C, and ^{15}N resonance assignments are given in the Supporting Information (Tables S2 and S3). Chemical shift index (CSI) analysis (*46*) on Hα, Cα, and Cβ resonances, the $^3J_{HNH\alpha}$ coupling constants, the $d_{\alpha N}(i-1,i)/d_{N\alpha}(i,i)$ ratios (*49*), and the NOEs patterns indicated the presence of seven α helices and one 3_{10} helix.

By analyzing the 3D ^{15}N-edited and ^{13}C-edited NOESY-HSQC spectra with the 2D NOESY spectrum, 3662 NOE cross-peaks were assigned and transformed into 2805 unique upper distance limits, of which 2320 were found to be meaningful (see Structure Calculation). These 2320 mean-ingful NOEs consisted of 283 intraresidue, 668 sequential, 783 medium-range, and 586 long-range NOEs. A plot of the number of meaningful NOEs per residue is shown in Figure 1; the average number of meaningful NOEs per residue is around 21. A total of 15 stereospecific proton pairs were obtained using the program GLOMSA (*28*). Distance re-straints, stereospecific assignments, and dihedral angles used in structure calculations are summarized in the Supporting Information.

Spectral Assignment of the Dy³⁺-Substituted Parvalbumin and Determination of PCS Restraints. Dy³⁺-substituted parvalbumin (CaDyPV) samples with Dy³⁺ replacing the Ca²⁺ ion in the C-terminal (EF) site (see below) were prepared by titration of the dicalcium parvalbumin (Ca-CaPV). The titration progress was followed by 2D ¹H−¹⁵N HSQC spectroscopy at 700 and 500 MHz. The achievement of the desired Dy³⁺:protein ratio could be easily monitored (*31, 33*), as cross-peaks of the CaCaPV form disappeared, while the new signals of the CaDyPV complex developed their full intensity. To avoid occupancy of other sites, the titration was stopped at a Dy³⁺:(Ca²⁺)₂-protein ratio of 0.9:1. In the 2D ¹H−¹⁵N HSQC spectrum, only cross-peaks from a single new species were observed, showing that the Dy³⁺ ion selectively occupies a single binding site out of the two Ca²⁺ sites of PV. It is well-known that lanthanides preferentially occupy the C-terminal (EF) site (*50, 51*) in PV. Therefore, the assignment strategy reported below relies on this assumption. However, the assumption is immediately validated by the excellent and univocal agreement of all the subsequent tensor and structure calculations with a C-terminal occupation.

The peaks of the 2D ¹H−¹⁵N spectrum of the CaDyPV were directly assigned in a semiautomated way using predictions based on the metal magnetic susceptibility anisotropy without additional spectral information. The metal−nuclei distances and the ratios between ¹H pseudo-contact shifts and ¹⁵N pseudocontact shifts ($\delta_H^{PC}/\delta_N^{PC}$) were considered for the assignment. These ratios were considered not to exceed the range 0.75−1.30 for all N−H groups that are farther than 12 Å from the metal (*52*). All possible candidate assignments for each peak were tabulated. Then the peaks having only one possible assignment were singled out, and their pseudocontact shifts (PCS) (*53−57*) were used to calculate initial metal magnetic susceptibility tensor parameters through eq 1 using the program FANTASIA (*58*).

$$PCS = \delta^{pc} = \frac{1}{12\pi r_i^3}\left[\Delta\chi^{para}_{ax}(3\cos^2\theta - 1) + \frac{3}{2}\Delta\chi^{para}_{rh}(\sin^2\theta\cos 2\Omega)\right] \quad (1)$$

With these tensor parameters, $\Delta\chi^{para}_{ax}$ and $\Delta\chi^{para}_{rh}$, predictions were made for the other shifted peaks, some of which could then be unambiguously identified in the spectrum, and included in a new magnetic tensor calculation. This iterative procedure was repeated until the assignments of as many peaks as possible were obtained. For the ambiguous assignments remaining, the intensity of the peaks and the direction of the paramagnetic shifts predicted by the program FANTASIA were also considered and used as a further criterion. Obviously, not all ¹H−¹⁵N HSQC cross-peaks could be detected in Dy³⁺-substituted parvalbumin due to the strong line broadening properties of Dy³⁺ (*31, 33*). In the end, out of 55 observed peaks, 53 NH cross-peaks for the backbone (corresponding to nearly 50% of the residues in PV) were assigned unambiguously. Two NH₂ cross-peaks for the side-chain amides were also assigned. The final magnetic susceptibility tensor parameters obtained are discussed later. Representative ¹H−¹⁵N HSQC spectra of CaCaPV and CaDyPV are shown in Figure 2.
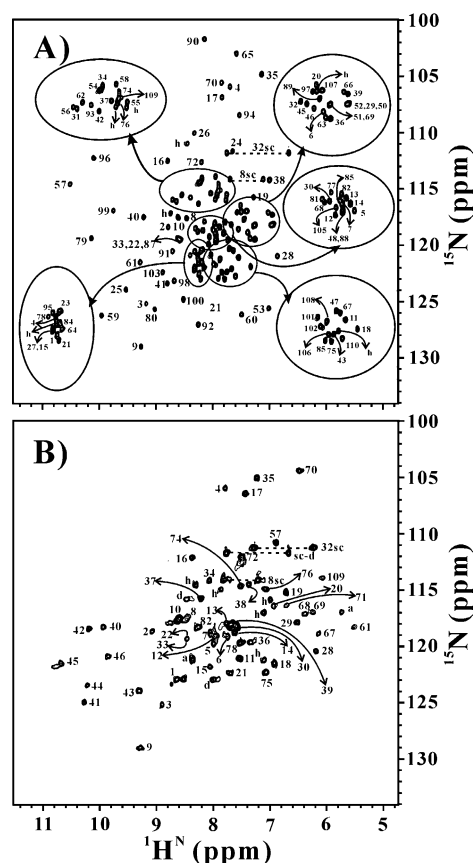

FIGURE 2: Representative ¹H−¹⁵N HSQC spectra at 298 K of CaCaPV (A) and CaDyPV (B). In (B), a indicates the two peaks with ambiguous assignment, h indicates peaks belonging to the His tag, and d indicates residual diamagnetic peaks. The C-terminus is also shown.

Determination of RDC Restraints. We exploit the orientation due to magnetic susceptibility anisotropy of the paramagnetic molecule (*59, 60*) for structural purposes, as first demonstrated by us in 1998 (*61*) and further shown more recently (*62−66*).

The contribution to RDC due to the magnetic susceptibility anisotropy tensor of the metal ion which is known from PCS analysis is refined as RDC^para. Such values for the CaDyPV derivative were determined by subtracting from the coupling constant measured for the backbone amide moiety of each residue the coupling constant measured for the same residue and at the same magnetic field in CaCaPV. The difference in RDC values between paramagnetic metal and diamagnetic metal ions (RDC^para) can then be expressed by

$$RDC^{para} = -[(^1J^{para} - {}^1J^{dia}) + (\delta^{para}_{DFS} - \delta^{dia}_{DFS})] \quad (2)$$

where δ_{DFS}^{para} and δ_{DFS}^{dia} are the paramagnetic and diamagnetic contributions to the dynamic frequency shifts (*67, 68*). The negative sign in eq 2 takes into account that the ¹J_NH scalar coupling is negative (*59*), while it is customary to report experimental ¹J_NH values with a positive sign. The magnitude of the δ_{DFS} values has been a matter of debate, but a correct equation (*69, 70*) predicts small values which, anyway, decrease with the third power of the distance from the metal ion. We then neglect the second term of RDC^para (*61, 62*).

A total of 47 RDC values were determined. These RDC are evenly distributed along the PV sequence. One or more

Table 1: Restraints Used in the Structural Calculations and the Final Resulting Target Function Together with Mean RMSD Values for the Backbone and All Heavy Atoms

diamagnetic restraints	paramagnetic restraints	target function (Å^2)					mean RMSD (Å)[a,b]	
		diamagnetic restraints	VDW[c]	PCS	RDC	total	backbone	heavy atoms
2320 NOEs, 16 H-bonds, 63 ϕ angles, 65 ψ angles		0.26	0.22			0.48 ± 0.09	0.55 ± 0.08	1.02 ± 0.08
2320 NOEs, 16 H-bonds, 63 ϕ angles, 65 ψ angles	112 PCS	0.30	0.30	0.24		0.84 ± 0.12	0.46 ± 0.06	0.96 ± 0.06
2320 NOEs, 16 H-bonds, 63 ϕ angles, 65 ψ angles	112 PCS, 47 RDC	0.39	0.36	0.25	0.10	1.09 ± 0.18	0.39 ± 0.05	0.90 ± 0.06

[a] For 20 structures. [b] Residues 5−106. [c] Target function for van der Waals violations.

RDC values are available for each stretch of 10 residues across the whole protein, except in the stretch corresponding to the Dy^{3+}-binding site (residues 91−102).

The paramagnetic RDC^{para} contribution to the $^1J_{NH}$ splitting can be expressed by the equation (*61, 62*):

$$RDC^{para} = -\frac{1}{4\pi} \frac{B_0^2}{15kT} \frac{\gamma_H \gamma_N h}{4\pi^2 r_{HN}^3} \Big[\Delta\chi^{para}_{ax}(3\cos^2\theta - 1) + \frac{3}{2}\Delta\chi^{para}_{rh}(\sin^2\theta\cos 2\phi) \Big] \quad (3)$$

where $\Delta\chi^{para}_{ax}$ and $\Delta\chi^{para}_{rh}$ are the axial and rhombic components of the metal magnetic susceptibility tensor of the metal determined in the previous section and θ and ϕ are the cylindric coordinates describing the orientation of the N−H bond vector within the principal axis system of the χ^{para} tensor. r_{HN} is the length of the N−H bond. All other symbols have their usual meaning. Equation 3 is used for structural calculation as implemented in the RDCDYANA-ORIENT module of the PARAMAGNETIC-DYANA suite of modules (see later) (*30, 62*).

R₁, R₂, and NOE Data. The NMR experiments for ^{15}N relaxation rates were performed at 600 MHz spectrometer and two temperatures (283 and 298 K). Average R_1, R_2, and $^1H–^{15}N$ NOE values are 1.46 ± 0.02 s^{-1}, 12.4 ± 0.2 s^{-1}, and 0.77 ± 0.16, respectively, at 283 K and 2.09 ± 0.03 s^{-1}, 8.41 ± 0.15 s^{-1}, and 0.70 ± 0.10, respectively, at 298 K. These values are consistent with a monomer of molecular mass 12 kDa. The R_1, R_2, and $^1H–^{15}N$ NOE values at the two temperatures are relatively similar throughout the sequence. This indicates that this protein has no regions showing large flexibility.

Structure Calculation. A total of 3662 NOESY cross-peaks were integrated, from which 2320 were found to be meaningful. The large difference is almost entirely due to intraresidue peaks and to a few longer range peaks that have very low intensity. With these 2320 meaningful NOEs, 63 ϕ and 65 ψ dihedral angles, 16 hydrogen bonds, and 15 stereospecific proton pairs were used as diamagnetic constraints in the structural calculation. For the family of 20 conformers obtained from diamagnetic constraints only, the mean RMSD values for the backbone and all heavy atoms after restrained energy minimization (REM) (*36*) are 0.55 ± 0.08 and 1.02 ± 0.07 Å,[2] respectively. If segments 20−25, 53−55, 66−67, and 92−96 are not included, the RMSD values drop to 0.44 ± 0.08 and 0.93 ± 0.08 for the backbone and heavy atoms, respectively.

By comparison of the spectra of the CaCaPV and CaDyPV derivatives 112 PCS (53 NH cross-peaks for the backbone and 2 NH_2 cross-peaks for the side-chain amide) and 47 RDC values were determined as paramagnetic restraints. First, only 112 PCS values were added to structural calculations as paramagnetic restraints using the PSEUDYANA module and refining the $\Delta\chi^{para}_{ax}$ and $\Delta\chi^{para}_{rh}$ parameters recalculated through FANTASIA by iteration. For the family of 20 conformers obtained with 112 PCS and all diamagnetic restraints, the mean backbone RMSD value was 0.46 ± 0.06 Å (whereas the RMSD value for the family obtained with diamagnetic restraints only was 0.55 ± 0.08 Å; see above and Figure 4). Therefore, by using PCS the quality of structure obtained was improved by about 20%. Then the 47 RDC values were added as paramagnetic restraints together with the 112 PCS using both the PSEUDYANA and RDCDYANA-ORIENT modules and again refining the $\Delta\chi^{para}_{ax}$ and $\Delta\chi^{para}_{rh}$ by iteration. Also, in this case the program FANTASIA was used; i.e., the refinement of the $\Delta\chi^{para}_{ax}$ and $\Delta\chi^{para}_{rh}$ was made by refining only on PCS and not on RDC values. The final resulting structure consists of 20 conformers with a target function of 1.09 ± 0.18 and the RMSD values from the mean of 0.39 ± 0.05 and 0.90 ± 0.06 Å for the backbone and all heavy atoms, respectively. Compared with the structure obtained by using the PCS values only as the paramagnetic restraints, the quality of the structure obtained by using both of the PCS and RDC values was improved again by about 15%. All restraints used in the structural calculations and the final resulting target function together with mean RMSD values for the backbone and all heavy atoms are summarized in Table 1. In this table, the decomposition of the target functions into contributions from each type of restraint is also shown. Of course, the target function for the diamagnetic restraints increased slightly by adding PCS values and then by adding both PCS and RDC values. All target functions for each type of restraint are less than 0.4, with no consistent violations.

The structure of human parvalbumin appears to be characterized by the following secondary structure elements: α1 (9−19), α2 (27−33), α3 (36−38), α4 (41−51), β1 (59), α5 (61−64), α6 (68−71), α7 (80−91), β2 (98), and α8 (100−109). Therefore, the protein contains seven α helices, one 3₁₀ helix, and three hydrogen-bonded turns. Earlier reported structural studies (*71*) on α-lineage parvalbumin revealed the folding of the polypeptide chain in mainly six helical segments named as AB, CD, and EF hands. The high-affinity metal-binding sites reside in CD and EF hands, whereas the AB site is unable to bind metal (*71*). Among all the nonhelical segments of human parvalbumin, loop 3 (residues 52−60) is the first metal-binding site and loop 5 (residues 92−99) is the second metal-binding site. These two

---

[2] The error in these and in all of the RMSD values reported hereafter represents only the spread of the local RMSD values across the family of the structures (*29*).
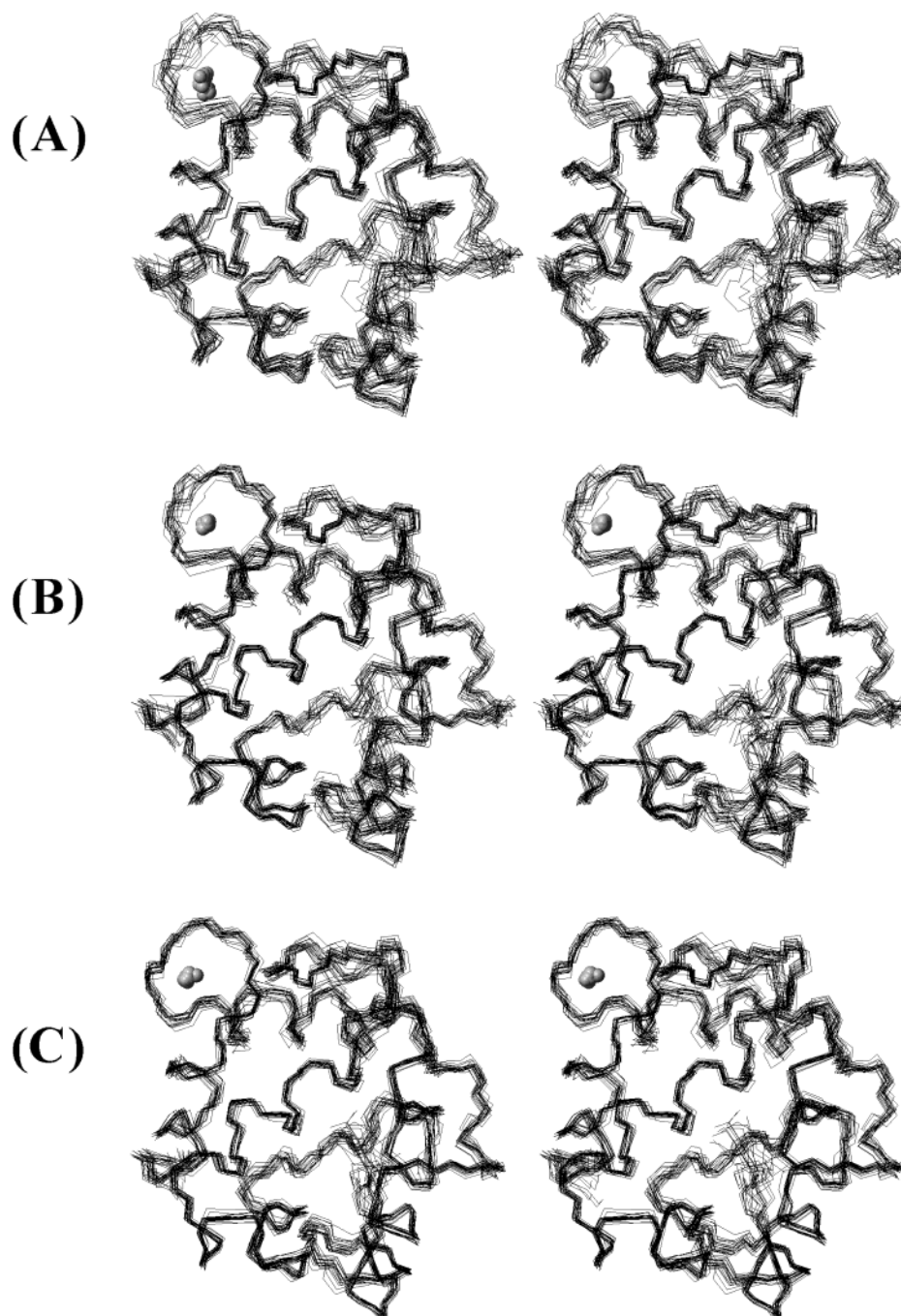
FIGURE 3: Stereoviews of the families of 20 conformers obtained by diamagnetic restraints only (A), with PCS (B), and with both PCS and RDC (C).

consecutive EF hands form a short antiparallel β sheet which is typical of well-formed EF-hand pairs (*72*).

Figure 3 illustrates stereoviews of the familes of 20 conformers obtained by diamagnetic constraints only, diamagnetic constraints with PCS values, and diamagnetic constraints with both PCS and RDC values. The improvement of quality of the structure obtained by using both PCS and RDC values is apparent and is not restricted to particular protein regions.

Determination of Magnetic Susceptibility Tensor Anisotropy Parameters. Magnetic susceptibility tensor parameters were obtained from preliminary DYANA structures and 112 PCS using the program FANTASIA (*58*) and recalculated iteratively during the structure refinement until convergence. For the RDC values, the paramagnetic tensor parameters

$\Delta\chi^{para}_{ax}$ and $\Delta\chi^{para}_{rh}$ obtained and recalculated iteratively from the PCS (and not from the RDC themselves) were always imposed. This procedure was suggested by our previous experiences of structural refinement using PCS and RDC separately, where the tensor back-calculated from RDC was always more variable than that back-calculated from PCS and converged much more slowly to a final value in agreement with both restraints. The $\Delta\chi^{para}_{ax}$ and $\Delta\chi^{para}_{rh}$ values of the magnetic susceptibility tensor parameters for the final resulting structure were $(29.6 \pm 0.3) \times 10^{-32}$ and $(12.1 \pm 0.2) \times 10^{-32}$ m^3, respectively, whereas for the structure obtained by 112 PCS with all diamagnetic restraints these values were $(29.4 \pm 0.5) \times 10^{-32}$ and $(9.81 \pm 0.24) \times 10^{-32}$ m^3, respectively. During the structural refinement by iteration, after adding RDC values as paramagnetic

restraints, the $\Delta\chi^{para}_{ax}$ value first decreased, then increased again, and finally converged to almost the same value of the initial stage. On the other hand, the $\Delta\chi^{para}_{rh}$ value increased continuously and then converged to $(12.1 \pm 0.2) \times 10^{-32}$ m³, which is more than 20% larger than the initial value. It seems that the $\Delta\chi^{para}_{ax}$ value is more influenced by the PCS restraints than indirectly by the RDC restraints, while the $\Delta\chi^{para}_{rh}$ value is more influenced indirectly by the RDC than by the PCS. This behavior is due to the different functional form of the two restraints (*33*) and is extensively analyzed in the Discussion section.

DISCUSSION

Structural Calculation and Assessment of the Paramagnetism-Based Refinement Strategy. Human parvalbumin consists of 110 amino acids (ca. 12 kDa) and includes three EF hands. For the structural calculation, a total of 2320 meaningful NOEs (i.e., about 21 NOEs/residue), 63 ϕ and 65 ψ dihedral angles, 16 hydrogen bonds, 15 stereospecific proton pairs, 112 PCS, and 47 RDC were used in DYANA calculations using the PSEUDYANA and RDCDYANA-ORIENT modules (*30*). The final resulting structure consists of 20 conformers with a target function of 1.09 ± 0.18 and RMSD values from the mean of 0.39 ± 0.05 and 0.90 ± 0.06 Å for the backbone and all heavy atoms, respectively, whereas the target function and the backbone RMSD values for the family obtained with only diamagnetic restraints were 0.48 ± 0.09 and 0.55 ± 0.08 Å, respectively. This indicates that the quality of the final resulting structure was quite improved by the contribution of PCS and RDC. Table 1 illustrates the various contributions to the target function for the diamagnetic and paramagnetic restraints. The increase in violation by adding PCS restraints is small and within the statistics, in the sense that the increase from 0.48 to 0.60 Å is not coming from consistent violations and is shared almost equally between NOEs and van der Waals restraints. The PCS target is also of the same magnitude as the other targets, so the restraints are well balanced. Similarly, introduction of RDC increases the contribution to the target from the other restraints by only 0.15 Å, with no consistent violation. Overall, the contribution from the diamagnetic restraints (including van der Waals violations) increases only from 0.48 to 0.75 Å upon addition of all the paramagnetic restraints, indicating that the two sets of restraints are in good agreement with one another. In turn, this confirms that the structure of the protein is maintained unaltered within experimental uncertainty upon lanthanide substitution. This increase of the violations of nonparamagnetic restraints appears evenly among all nonhelical sites and almost does not appear in all helical sites. The mean RMSD values per residue for the three structure families calculated using diamagnetic restraints only, diamagnetic restraints plus PCS values, and diamagnetic restraints plus both PCS and RDC values are shown in Figure 4. The improvement of the quality of the structure is apparent not only for the residues for which PCS or PCS and RDC values were available but also elsewhere. Particularly, all nonhelical parts, except the first Ca^{2+}-binding site (residues 52−63), were noticeably improved. Even the EF site itself, which holds the Dy^{3+} ion, is improved, despite no restraints being obtained in the immediate neighborhood of the metal. The RMSD for the metal ion itself (Ca^{2+} or
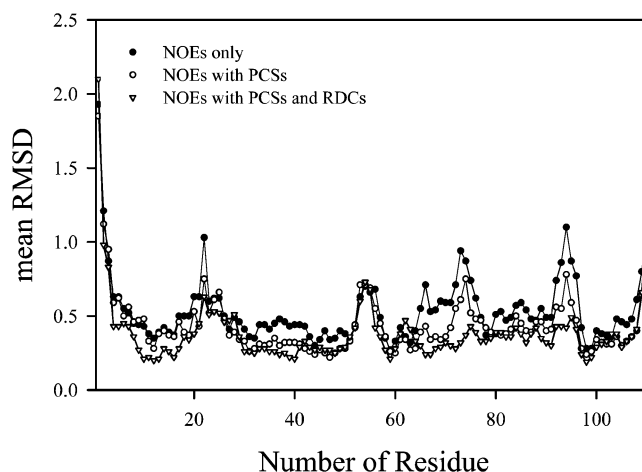

FIGURE 4: RMSD per residue for the families of 20 conformers obtained by diamagnetic restraints only (●), with PCS (○), and with both PCS and RDC (▽).

Dy^{3+}) passes from 0.63 ± 0.29 to 0.25 ± 0.10 to 0.26 ± 0.12 for the three families.

The different behavior of the PCS and RDC restraints is worthy of a detailed analysis. These restraints are available thanks to the favorable lanthanide-binding properties of calcium-binding proteins, including parvalbumins among many others. They require the recording of one 2D $^1H-^{15}N$ HSQC spectrum and one 3D NOESY-HSQC spectrum of the lanthanide (Dy^{3+} in this case) derivative to compare the shifts with those of the native protein under the same conditions in order to obtain the PCS values and measuring two sets of coupling constants (of, e.g., NH moieties) at the same field for the native and lanthanide-substituted protein in order to obtain the RDC values. As shown in the Results section and previously demonstrated (*62*, *64*, *73*), de novo assignment of the paramagnetic derivative is unnecessary, as most of the observed shifted peaks can be univocally assigned through predictions from the diamagnetic structure and initial tensor estimates, which are then refined through a few iteration cycles. In front of the relative easiness of obtaining these additional paramagnetism-based restraints, the improvement of the structure is noticeable, in terms of both precision (RMSD) and accuracy (overall agreement of sets of restraints of different nature). In this respect, the improvement of the precision is more pronounced when the PCS restraints are added to the diamagnetic ones than when RDC are added to the diamagnetic plus PCS restraints. On the other hand, the increase in accuracy, as judged by the improvement of the agreement with the newly introduced restraints, is modest for the PCS, which are already in good agreement with the diamagnetic structure, and dramatic for the RDC, which are very much scattered in the diamagnetic and in the diamagnetic plus PCS families. This behavior is illustrated in Figures 5 (PCS) and 6 (RDC). The correlation coefficient for the calculated vs observed PCS passes from 0.953 in the structure obtained without PCS restraints (Figure 5A) to 0.981 in the structure obtained with the inclusion of PCS (Figure 5B) and remains 0.981 in the structure obtained with the additional inclusion of RDC (Figure 5C). On the other hand, the correlation coefficient for the calculated vs observed RDC is very poor (0.598) for the structure obtained with diamagnetic plus PCS restraints (Figure 6A) and
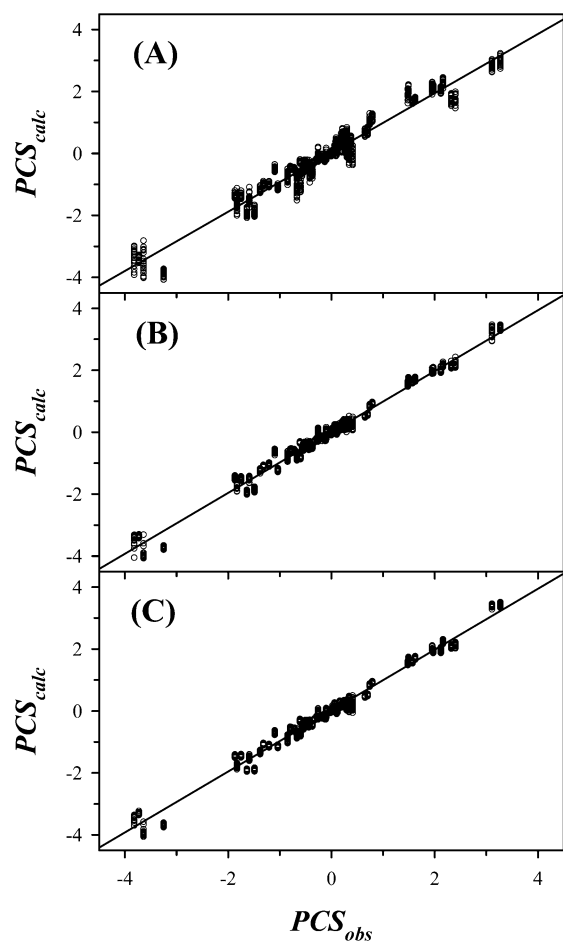
FIGURE 5: Plots of calculated versus experimental PCS values for the CaDyPV derivative. Calculated PCS were obtained from the families of 20 conformers determined by diamagnetic restraints only (A), with 112 PCS (B), and with both 112 PCS and 47 RDC values (C).
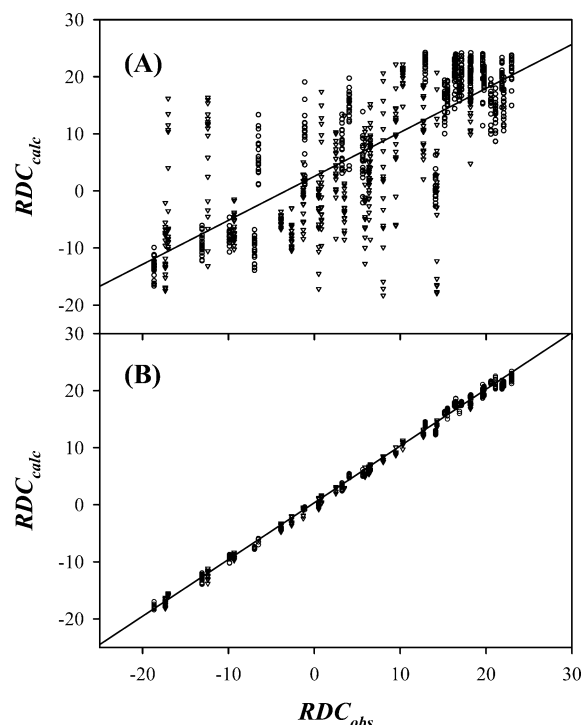

FIGURE 6: Plots of experimental versus calculated RDC values for the CaDyPV derivative. Calculated RDC were obtained from the families of 20 conformers, which were calculated without RDC (A) and with RDC (B) restraints, and paramagnetic tensor parameters obtained by PCS. The ○ and ▽ symbols refer to residues in helical sites and in nonhelical sites, respectively.

becomes excellent (0.996) after inclusion of RDC restraints (Figure 6B). As discussed earlier, introduction of RDC restraints does not introduce significant violations of any other restraints. The very poor correlation coefficient for the structure calculated without RDC values is apparently not due to a bad overall quality of the structure calculated without RDC values, which had already a satisfactory RMSD value. Rather, despite the large number of NOEs per residue, the scatter of the orientation of the NH vectors, especially in nonhelical regions, is very high. The RDC values are very influenced by even small changes of the θ and ϕ angles of the NH vectors. Indeed, also the agreement between the observed RDC values and those calculated from the X-ray structure of the rat parvalbumin (*38*) (at 2.0 Å resolution; PDB code 1RTP) is poor, despite the very high overall similarity of the two structures (see below).

In Figure 6A it is also apparent that the calculated RDC values in the loop regions as well as in the terminal regions are more spread out than those in the helical regions. The loop and terminal regions are often less constrained than the secondary structure regions in protein solution structures due to a lower number of experimental restraints. Therefore, the orientation of the NH vectors in the loop and terminal regions is expected to be less well defined. Most of the RDC contribution to the target function (0.10, Table 1) indeed arises from the RDC values in nonhelical regions. Peptide

nitrogen R_1, R_2, and NOE data show that the mobility of the nonhelical regions (at least in the nano- to picosecond time scale) is only modestly higher than in the helices, at variance with, for instance, the linker between the two EF hands in calbindin D_{9k} (*74*) or in the C-terminus of calmodulin (*75–77*). Therefore, intrinsic mobility can be only minimally responsible for the lower precision of nonhelical regions in the structure solved by using diamagnetic restraints only, and the lower precision must just arise from the lower number of restraints.

After incorporating the RDC restraints, the agreement between the observed and calculated PCS values increases only slightly (see Figure 5B,C). This means that the PCS values are very little influenced by the angles θ and ϕ defined by the NH vectors, especially at large distances from the metal. In this respect, the modest decrease of RMSD upon addition of RDC restraints does not do justice to their importance. The RMSD of the orientation of the NH vectors themselves would be a much better reporter.

Differences between Human and Rat Parvalbumin. The overall agreement between the 3D structure of human and rat parvalbumin (the latter at 2.0 Å resolution) is quite good, as expected from the high percentage of residue identity (87%) between the two orthologue proteins. However, local differences are apparent. A good way of looking at these differences is to compare the Ramachandran (*35*) values residue by residue. The overall quality of the solution structure determined in this work based on Ramachandran plots is quite good (about 81% of residues in most favored regions and 15% in additionally allowed regions). We found that for residues Leu 7, Ser 20, Pro73, Asp 74, and Ala 75 there are striking differences (e.g., from the A to the B region
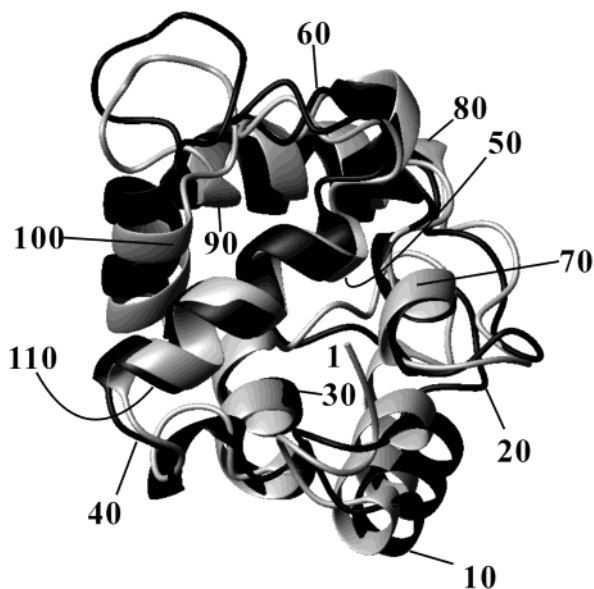
FIGURE 7: Ribbon representation of the final structure of human parvalbumin (black) versus the X-ray structure of rat parvalbumin (gray). The backbone RMSD between these two structures is 1.69 Å.

of the Ramachandran plane or vice versa) between the two structures. Furthermore, all of the differences are in the loops and not in the helices, as expected. However, some differences are at the beginning or the end of helices, in such a way that, e.g., one helix is shorter (or longer) in the rat (or in the human) or vice versa. A plot of the final resulting structure of human parvalbumin versus the X-ray structure of rat parvalbumin is shown in Figure 7.

In the case of Leu 7, which occurs before the first helix (residues 9−19), the Ramachandran plot shows that the ϕ and ψ angles of this residue are in the A region, whereas those of rat parvalbumin are in the B region. In this case, the residues that immediately follow in the sequence are different. The following residue of human parvalbumin is Asn 8, compared with Ser 8 in the rat protein. Inspection of the 3D structures suggests that this difference between the human and the rat proteins at position 7 arises from a different orientation of the Asn 8 and Ser 8 side chains.

Ser 20, which is just after the first helix (residues 9−19) and marks the beginning of the metal-devoided AB site, shows well-defined ϕ and ψ angles that are strikingly in the middle of the A and B regions. This should be compared with Thr 20 of the rat protein, which is clearly in the A region and therefore prolongs the first helix. Also, this difference corresponds to a place where differences in amino acids occur. Attempts to fix the ϕ and ψ angles of Ser 20 to either the A or the B regions resulted in a number of violations, especially angle violations, giving a large increase in both the target function and the local RMSD values.

A third difference between the two structures is observed at residues 73−75, which are just after the second helix of the CD site (residues 61−72). The ϕ and ψ angles place these residues in the B-L-A regions, respectively, whereas those of the rat protein are in the A-A-B regions, respectively. Residue 73 of the human protein is a *trans*-proline, instead of a serine in the rat protein. The ϕ and ψ angles of *trans*-proline are in the B region, and those of *cis*-proline are in the A region. Attempts to force Pro 73 to be in the cis

conformation to match the structure of the rat protein again resulted in a large increase of target function and local RMSD. Apparently, given the presence of a *trans*-proline 73 in the human protein, the following two amino acids have to take a Ramachandran L-A configuration rather than A-B to compensate for the perturbation introduced by Pro 73 and resume the same fold of the rat protein at residue 76 and beyond.

In summary, there are three distinct regions in human PV, around Asn 8, Ser 20, and Pro 73, that show a distinct change in the local fold with respect to rat parvalbumin, and in each of these three cases this difference is related to a difference in one amino acid between the two orthologue proteins. All of the differences discussed above between human and rat PV are outside the experimental uncertainty. It should be noted that these differences were already apparent in the solution structure before refinement using paramagnetic restraints but that the lower reliability of the latter, especially in the Ramachandran angles, would have made the whole comparison less reliable.

PV is the major known allergen in fish, fish proteins being among the most common causes of food allergy with IgE-mediated anaphylaxis (*78*). The availability of the human PV structure allows us to perform a whole protein comparison between the human and the fish proteins, in an attempt to understand the molecular basis of the human IgE reactivity toward fish PV. A seminal work on cod PV reported the region of reactivity to be located in amino acid segment 88−103 (*79*). This segment corresponds to the second metal-binding site of the protein (third EF-hand pair). The identification of this metal-binding region as the allergenic one would be consistent with the reported lower allergic potential of apo versus calcium-loaded carp PV (*80*), because of the local conformational change determined by the loss of metal-binding ability of PV. Surprisingly, however, the present structural data show that the 88−103 segment is the most conserved between carp and human PV in terms of both shape and surface charge distribution, while other shorter regions (i.e., amino acids 18−22, amino acids 75−79, or the cavity between amino acids 50−53 and 61−64) show much larger variability. There is still considerable debate regarding the structural determinants of allergy by aptenes (*81*), i.e., if they are due to shape and charge recognition of a structured region of the allergenic protein or to the conformational features of a denatured amino acid stretch. In the first case, the 88−103 segment loses attractiveness as a candidate, while in the second case it would be difficult to explain the lower allergic potential of apo versus calcium-loaded carp PV. In any case, the present structural data can represent a starting point for future investigations aimed at the experimental identification of fish PV IgE-reactive epitopes, useful for diagnosis, research, and therapeutic applications.

Another reason of biomedical interest in the present three-dimensional structure of human PV is the possibility of PV to become the target of structure-based design of small molecules able to modulate its Ca^{2+}-binding dynamics, opening a pharmacological approach to the repetitive GABA release in the GABAergic neuronal networks in which the protein is selectively expressed (*8*). Since these networks have been shown to be altered in the prefrontal cortex of subjects affected by schizophrenia (*82, 83*), possibly as an

effect of reduced expression of PV (*84*), modulation of PV activity could become of interest in psychiatry.

CONCLUDING REMARKS

The solution structure of human PV is here reported to a high degree of refinement. The strategy of using Dy^{3+} replacement for structural refinement has been further developed and automatized. The spectral assignment for the Dy^{3+} derivative is obtained on the basis of trial and error. PCS and RDC for a number of NH and NH_2 moieties have been used as restraints. RDC in particular have been used in an unprecedented way. This approach may pave the road for highly refined solution structure of calcium proteins. As a result, an instructive comparison could be performed with the orthologue structures from rat with 87% identity, which is available at 2 Å of resolution. A number of local variations are detected, which make this research valuable also from the structural biology point of view. The dynamic information will become precious in comparison with the members of the parvalbumin family. The availability of the structure of PVs represents a significant hint to understand the details of the biological function.

ACKNOWLEDGMENT

SUPPORTING INFORMATION AVAILABLE

Seven tables giving acquisition parameters for NMR experiments and ^1H, ^{15}N, and ^{13}C assignments for human parvalbumin, stereospecific assignment for diastereomeric pairs and ϕ and ψ torsional angle restraints of parvalbumin, and PCS and RDC values used in solution structure calculations for Dy^{3+}-substituted parvalbumin. This material is available free of charge via the Internet at http://pubs.acs.org.

REFERENCES

1. Berridge, M. J., Bootman, M. D., and Roderick, H. L. (2003) Calcium signalling: dynamics, homeostasis and remodelling, *Nat. Rev. Mol. Cell. Biol. 4*, 517–529.
2. Baimbridge, K. G., Celio, M. R., and Rogers, J. H. (1992) Calcium-binding proteins in the nervous system, *Trends Neurosci. 15*, 303–308.
3. Ulfig, N. (2002) Calcium-binding proteins in the human developing brain, *Adv. Anat., Embryol. Cell Biol. 165* (III–IX), 1–92.
4. Schwaller, B., Meyer, M., and Schiffmann, S. (2002) "New" functions for "old" proteins: the role of the calcium-binding proteins calbindin D_{28k}, calretinin and parvalbumin, in cerebellar physiology. Studies with knockout mice, *Cerebellum 1*, 241–258.
5. Berchtold, M. W. (1995) *Parvalbumin and Oncomodulin*, pp 123–128, Oxford University Press, Oxford, U.K.
6. Wnuk, W., Cox, J. A., and Stein, E. A. (1982) Parvalbumins and other soluble high-affinity calcium-binding proteins from muscle, in *Calcium & Cell Function* (Cheung, W. Y., Ed.) Vol. 2, pp 243–278, Academic Press, New York.
7. Schwaller, B., Dick, J., Dhoot, G., Carroll, S., Vrbova, G., Nicotera, P., Pette, D., Wyss, A., Bluethmann, H., Hunziker, W., and Celio, M. R. (1999) Prolonged contraction-relaxation cycle of fast-twitch muscles in parvalbumin knockout mice, *Am. J. Physiol. 276*, C395–C403.
8. Vreugdenhil, M., Jefferys, J. G., Celio, M. R., and Schwaller, B. (2003) Parvalbumin-deficiency facilitates repetitive IPSCs and gamma oscillations in the hippocampus, *J. Neurophysiol. 89*, 1414–1422.
9. Galarreta, M., and Hestrin, S. (2002) Electrical and chemical synapses among parvalbumin fast-spiking GABAergic inter-neurons in adult mouse neocortex, *Proc. Natl. Acad. Sci. U.S.A. 99*, 12438–12443.
10. Chou, J. J., Li, S., and Bax, A. (2000) Study of conformational rearrangement and refinement of structural homology models by the use of heteronuclear dipolar couplings, *J. Biomol. NMR 18*, 217–227.
11. Ahmed, F. R., Rose, D. R., Evans, S. V., Pippy, M. E., and To, R. (1993) Refinement of recombinant oncomodulin at 1.30 Å resolution, *J. Mol. Biol. 230*, 1216–1224.
12. Ahmed, F. R., Przybylska, M., Rose, D. R., Birnbaum, G. I., Pippy, M. E., and MacManus, J. P. (1990) Structure of oncomodulin refined at 1.85 Å resolution. An example of extensive molecular aggregation via Ca^{2+}, *J. Mol. Biol. 216*, 127–140.
13. McPhalen, C. A., Sielecki, A. R., Santarsiero, B. D., and James, M. N. (1994) Refined crystal structure of rat parvalbumin, a mammalian alpha-lineage parvalbumin, at 2.0 Å resolution, *J. Mol. Biol. 235*, 718–732.
14. Bruno, J., Horrocks, W. D., Jr., and Zauhar, R. J. (1992) Europium-(III) luminescence and tyrosine to terbium(III) energy-transfer studies of invertebrate (octopus) calmodulin, *Biochemistry 31*, 7016–7026.
15. Eccles, C., Güntert, P., Billeter, M., and Wüthrich, K. (1991) Efficient analysis of protein 2D NMR spectra using the software package EASY, *J. Biomol. NMR 1*, 111–130.
16. Piotto, M., Saudek, V., and Sklenar, V. (1992) Gradient-tailored excitation for single-quantum NMR spectroscopy of aqueous solutions, *J. Biomol. NMR 2*, 661–665.
17. Bertini, I., Ciurli, S., Dikiy, A., and Luchinat, C. (1993) Electronic structure of the $[Fe_4Se_4]^{3+}$ clusters in *Chromatium vinosum* HiPIP and *Ectothiorhodospiza halophila* HiPIP II through NMR and EPR studies, *J. Am. Chem. Soc. 115*, 12020–12028.
18. Schleucher, J., Schwendinger, M., Sattler, M., Schmidt, P., Schedletzky, O., Glaser, S. J., Sorensen, O. W., and Griesinger, C. (1994) A general enhancement scheme in heteronuclear multidimensional NMR employing pulsed field gradients, *J. Biomol. NMR 4*, 301–306.
19. Tjandra, N., Grzesiek, S., and Bax, A. (1996) Magnetic field dependence of nitrogen-proton *J* splittings in ^{15}N-enriched human Ubiquitin resulting from relaxation interference and residual dipolar coupling, *J. Am. Chem. Soc. 118*, 6264–6272.
20. Ottiger, M., Delaglio, F., and Bax, A. (1998) Measurement of *J* and dipolar couplings from simplified two-dimensional NMR spectra, *J. Magn. Reson. 131*, 373–378.
21. Grzesiek, S., and Bax, A. (1993) The importance of not saturating H_2O in protein NMR. Application to sensitivity enhancement and NOE measurements, *J. Am. Chem. Soc. 115*, 12593–12594.
22. Marion, D., and Wüthrich, K. (1983) Application of phase sensitive correlated spectroscopy (COSY) for measurements of proton–proton spin–spin coupling constants in proteins, *Biochem. Bio-phys. Res. Commun. 113*, 967–974.
23. Kay, L. E., Nicholson, L. K., Delaglio, F., Bax, A., and Torchia, D. A. (1992) Pulse sequences for removal of the effects of cross correlation between dipolar and chemical-shift anisotropy relax-ation mechanisms on the measurement of heteronuclear T_1 and T_2 values in proteins, *J. Magn. Reson. 97*, 359–375.
24. Kay, L. E., Torchia, D. A., and Bax, A. (1989) Backbone dynamics of proteins as studied by ^{15}N inverse detected heteronuclear NMR spectroscopy: application to staphylococcal nuclease, *Biochemistry 28*, 8972–8979.
25. Marquardt, D. W. (1963) An algorithm for least-squares estimation of nonlinear parameters, *J. Soc. Ind. Appl. Math. 11*, 431–441.
26. Press, W. H., Flannery, B. P., Teukolsky, S. A., and Vetterling, W. T. (1988) in *Numerical Recipes in C—The Art of Scientific Computing*, Cambridge University Press, New York.
27. Palmer, A. G., III, Rance, M., and Wright, P. E. (1991) Intramo-lecular motions of a zinc finger DNA-binding domain Xfin characterized by proton-detected natural abundance ^{13}C hetero-nuclear NMR spectroscopy, *J. Am. Chem. Soc. 113*, 4371–4380.
28. Güntert, P., Braun, W., and Wüthrich, K. (1991) Efficient computation of three-dimensional protein structures in solution from Nuclear Magnetic Resonance data using the program DIANA and the supporting programs CALIBA, HABAS and GLOMSA, *J. Mol. Biol. 217*, 517–530.
29. Güntert, P., Mumenthaler, C., and Wüthrich, K. (1997) Torsion Angle Dynamics for NMR Structure Calculation with the new program DYANA, *J. Mol. Biol. 273*, 283–298.
30. The source codes of the modules PSEUDYANA and RDCDYANA-ORIENT are available at www.postgenomicnmr.net. They are implemented in the program PARAMAGNETIC-DYANA, which can be obtained through www.postgenomicnmr.net by those who already have a licensed

version of DYANA [ETH, Zurich; see Güntert, P., Mumenthaler, C., and Wüthrich, K. (1997) *J. Mol. Biol. 273*, 283−298]. The program FANTASIA can be freely downloaded from www.postgenomicnmr.net.

31. Allegrozzi, M., Bertini, I., Janik, M. B. L., Lee, Y.-M., Liu, G., and Luchinat, C. (2000) Lanthanide-induced pseudocontact shifts for solution structure refinements of macromolecules in shells up to 40 Å from the metal ion, *J. Am. Chem. Soc. 122*, 4154−4161.

32. Bertini, I., Lee, Y.-M., Luchinat, C., Piccioli, M., and Poggi, L. (2001) Locating the metal ion in calcium-binding proteins by using cerium(III) as a probe, *ChemBioChem 2*, 550−558.

33. Bertini, I., Janik, M. B. L., Lee, Y.-M., Luchinat, C., and Rosato, A. (2001) Magnetic susceptibility tensor anisotropies for a lanthanide ion series in a fixed protein matrix, *J. Am. Chem. Soc. 123*, 4181−4188.

34. Koradi, R., Billeter, M., and Wüthrich, K. (1996) MOLMOL: a program for display and analysis of macromolecular structures, *J. Mol. Graphics 14*, 51−55.

35. Laskowski, R. A., MacArthur, M. W., Moss, D. S., and Thornton, J. M. (1993) PROCHECK: a program to check the stereochemical quality of protein structures, *J. Appl. Crystallogr. 26*, 283−291.

36. Pearlman, D. A., Case, D. A., Caldwell, J. W., Ross, W. S., Cheatham, T. E., Ferguson, D. M., Seibel, G. L., Singh, U. C., Weiner, P. K., and Kollman, P. A. (1997) in AMBER 5.0, University of California, San Francisco.

37. Sali, A., Potterton, L., Yuan, F., van Vlijmen, H., and Karplus, M. (1995) Evaluation of comparative protein modeling by MODELLER, *Proteins: Struct., Funct., Genet. 23*, 318−326.

38. McPhalen, C. A., Sielecki, A. R., Santarsiero, B. D., and James, M. N. (1994) Refined crystal structure of rat parvalbumin, a mammalian α-lineage parvalbumin, at 2.0 Å resolution, *J. Mol. Biol. 235*, 718−732.

39. Grzesiek, S., and Bax, A. (1992) An efficient experiment for sequential backbone assignment of medium-sized isotopically enriched proteins, *J. Magn. Reson. 99*, 201−207.

40. Muhandiram, D. R., and Kay, L. E. (1994) Gradient-enhanced triple resonance three-dimensional NMR experiments with improved sensitivity, *J. Magn. Reson., Ser. B 103*, 203-216.

41. Carlomagno, T., Maurer, M., Sattler, M., Schwendinger, M. G., Glaser, S. J., and Griesinger, C. (1996) PLUSH TACSY: homonuclear planar TACSY with two-band selective shaped pulses applied to C_α, C′ transfer and C_β, $C_{aromatic}$ correlations, *J. Biomol. NMR 8*, 161−170.

42. Kay, L. E., Xu, G. Y., Singer, A. U., Muhandiram, D. R., and Forman-Kay, J. D. (1993) A gradient-enhanced HCCH-TOCSY experiment for recording side-chains ^{1}H and ^{13}C correlations in H_2O samples of proteins, *J. Magn. Reson., Ser. B 101*, 333−337.

43. Wider, G., Neri, D., Otting, G., and Wüthrich, K. (1989) A heteronuclear three-dimensional NMR experiment for measurements of small heteronuclear coupling constants in biological macromolecules, *J. Magn. Reson. 85*, 426−431.

44. Hwang, T. L., and Shaka, A. J. (1995) Water suppression that works. Excitation sculpting using arbitrary waveforms and pulsed field gradients, *J. Magn. Reson., Ser. A 112*, 275−279.

45. Kuboniwa, H., Grzesiek, S., Delaglio, F., and Bax, A. (1994) Measurement of HN−Hα *J* couplings in calcium-free calmodulin using new 2D and 3D water-flip-back methods, *J. Biomol. NMR 4*, 871−878.

46. Wishart, D. S., and Sykes, B. D. (1994) The ^{13}C chemical-shift index: a simple method for the identification of protein secondary structure using ^{13}C chemical-shift data, *J. Biomol. NMR 4*, 171−180.

47. Vuister, G. W., and Bax, A. (1993) Quantitative J correlation: a new approach for measuring homonuclear three-bond $J(H^NH^\alpha)$ coupling constants in ^{15}N-enriched proteins, *J. Am. Chem. Soc. 115*, 7772−7777.

48. Kay, L. E., Xu, G. Y., and Yamazaki, T. (1994) Enhanced-sensitivity triple-resonance spectroscopy with minimal H_2O saturation, *J. Magn. Reson., Ser. A 109*, 129−133.

49. Gagné, S. M., Tsuda, S., Li, M. X., Chandra, M., Smillie, L. B., and Sykes, B. D. (1994) Quantification of the calcium-induced secondary structural changes in the regulatory domain of troponin-C, *Protein Sci. 3*, 1961−1974.

50. Lee, L., and Sykes, B. D. (1983) Use of lanthanide-induced nuclear magnetic resonance shifts for determination of protein structure in solution: EF calcium binding site of carp parvalbumin, *Biochemistry 22*, 4366−4373.

51. Capozzi, F., Cremonini, M. A., Luchinat, C., and Sola, M. (1993) Assignment of pseudo-contact-shifted ^{1}H NMR resonances in the EF-site of Yb^{3+}-substituted rabbit parvalbumin through a combination of 2D techniques and magnetic susceptibility tensor determination, *Magn. Reson. Chem. 31*, S118−S127.

52. Allegrozzi, M., Bertini, I., Choi, S.-N., Lee, Y.-M., and Luchinat, C. (2002) Detecting small structural changes in metalloproteins by the use of NMR pseudocontact shifts, *Eur. J. Inorg. Chem.* 2121−2127.

53. McConnell, H. M., and Robertson, R. E. (1958) Isotropic nuclear resonance shifts, *J. Chem. Phys. 29*, 1361−1365.

54. Kurland, R. J., and McGarvey, B. R. (1970) Isotropic NMR shifts in transition metal complexes: calculation of the Fermi contact and pseudocontact terms, *J. Magn. Reson. 2*, 286−301.

55. Banci, L., Bertini, I., Bren, K. L., Cremonini, M. A., Gray, H. B., Luchinat, C., and Turano, P. (1996) The use of pseudocontact shifts to refine solution structures of paramagnetic metalloproteins: Met80Ala cyano-cytochrome *c* as an example, *J. Biol. Inorg. Chem. 1*, 117−126.

56. Bertini, I., and Luchinat, C. (1996) in *NMR of paramagnetic substances*, Elsevier, Amsterdam.

57. Bertini, I., Luchinat, C., and Parigi, G. (2001) in *Solution NMR of Paramagnetic Molecules*, Elsevier, Amsterdam.

58. Banci, L., Bertini, I., Gori Savellini, G., Romagnoli, A., Turano, P., Cremonini, M. A., Luchinat, C., and Gray, H. B. (1997) Pseudocontact shifts as constraints for energy minimization and molecular dynamic calculations on solution structures of paramagnetic metalloproteins, *Proteins: Struct., Funct., Genet. 29*, 68−76.

59. Tolman, J. R., Flanagan, J. M., Kennedy, M. A., and Prestegard, J. H. (1995) Nuclear magnetic dipole interactions in field-oriented proteins: information for structure determination in solution, *Proc. Natl. Acad. Sci. U.S.A. 92*, 9279−9283.

60. Tjandra, N., and Bax, A. (1997) Direct measurement of distances and angles in biomolecules by NMR in a dilute liquid crystalline medium, *Science 278*, 1111−1114.

61. Banci, L., Bertini, I., Huber, J. G., Luchinat, C., and Rosato, A. (1998) Partial orientation of oxidized and reduced cytochrome b_5 at high magnetic fields: Magnetic susceptibility anisotropy contributions and consequences for protein solution structure determination, *J. Am. Chem. Soc. 120*, 12903−12909.

62. Barbieri, R., Bertini, I., Cavallaro, G., Lee, Y.-M., Luchinat, C., and Rosato, A. (2002) Paramagnetically induced residual dipolar couplings for solution structure determination of lanthanide binding proteins, *J. Am. Chem. Soc. 124*, 5581−5587.

63. de Alba, E., Suzuki, M., and Tjandra, N. (2001) Simple multidimensional NMR experiments to obtain different types of one-bond dipolar couplings simultaneously, *J. Biomol. NMR 19*, 63−67.

64. Barbieri, R., Bertini, I., Lee, Y.-M., Luchinat, C., and Velders A. H. (2002) Structure-independent cross-validation between residual dipolar couplings originating from internal and external orienting media, *J. Biomol. NMR 22*, 365−368.

65. Choy, W.-Y., Tollinger, M., Mueller, G. A., and Kay, L. E. (2001) Direct structure refinement of high molecular weight proteins against residual dipolar couplings and carbonyl chemical shift changes upon alignment: an application to maltose binding protein, *J. Biomol. NMR 21*, 31−40.

66. Tolman, J. R. (2002) A novel approach to the retrieval of structural and dynamic information from residual dipolar couplings using several oriented media in biomolecular NMR spectroscopy, *J. Am. Chem. Soc. 124*, 12020−12030.

67. Szebenyi, D. M. E., and Moffat, K. (1986) The refined structure of vitamin D-dependent calcium-binding protein from bovine intestine. Molecular details, ion binding, and implications for the structure of other calcium-binding proteins, *J. Biol. Chem. 261*, 8761−8777.

68. Akke, M., Skelton, N. J., Kördel, J., Palmer, A. G., III, and Chazin, W. J. (1993) Effects of ion binding on the backbone dynamics of calbindin D_{9k} determined by ^{15}N NMR relaxation, *Biochemistry 32*, 9832−9844.

69. Bertini, I., Luchinat, C., and Parigi, G. (2002) Paramagnetic constraints. An aid for quick solution structure determination of paramagnetic metalloproteins, *Concepts Magn. Reson. 14*, 259−286.

70. Banci, L., Bertini, I., Cavallaro, G., Giachetti, A., Luchinat, C., and Parigi, G. (2004) Paramagnetism-based restraints for Xplor-NIH, *J. Biomol. NMR 28*, 249−261.

71. Pauls, T. L., Cox, J. A., and Berchtold, M. W. (1996) The Ca^{2+}-binding proteins. Parvalbumin and oncomodulin and their genes:

new structural and functional findings, *Biochim. Biophys. Acta 1306*, 39−54.

72. Kretsinger, R. H., and Nockolds, C. E. (1973) Carp muscle calcium-binding protein. II. Structure determination and general description, *J. Biol. Chem. 248*, 3313−3326.

73. Bertini, I., Janik, M. B. L., Liu, G., Luchinat, C., and Rosato, A. (2001) Solution structure calculations through self-orientation in a magnetic field of cerium(III) substituted calcium-binding protein, *J. Magn. Reson. 148*, 23−30.

74. Bertini, I., Carrano, C. J., Luchinat, C., Piccioli, M., and Poggi, L. (2002) A ^{15}N NMR mobility study on the dicalcium P43M calbindin D_{9k} and its mono-La^{3+}-substituted form, *Biochemistry 41*, 5104−5111.

75. Barbato, G., Ikura, M., Kay, L. E., Pastor, R. W., and Bax, A. (1992) Backbone dynamics of calmodulin studied by ^{15}N relaxation using inverse detected two-dimensional NMR spectroscopy; the central helix is flexible, *Biochemistry 31*, 5269−5278.

76. Evenäs, J., Forsén, S., Malmendal, A., and Akke, M. (1999) Backbone dynamics and energetics of a calmodulin domain mutant exchanging between closed and open conformations, *J. Mol. Biol. 289*, 603−617.

77. Baber, J. L., Szabo, A., and Tjandra, N. (2001) Analysis of slow interdomain motion of macromolecules using NMR relaxation data, *J. Am. Chem. Soc. 123*, 3953−3959.

78. Sampson, H. A., and Metcalfe, D. D. (1992) Food allergies, *J. Am. Med. Assoc. 268*, 2840−2844.

79. Elsayed, S., Ragnarsson, U., Apold, J., Florvaag, E., and Vik, H. (1981) Allergenic synthetic peptide corresponding to the second calcium-binding loop of cod allergen M, *Scand. J. Immunol. 14*, 207−211.

80. Bugajska-Schretter, A., Grote, M., Vangelista, L., Valent, P., Sperr, W. R., and Rumpold, H. (2000) Purification, biochemical, and immunological characterisation of a major food allergen: different immunoglobulin E recognition of the apo- and calcium-bound forms of carp parvalbumin, *Gut 46*, 661−669.

81. Aalberse, R. C. (2000) Structural biology of allergens, *J. Allergy Clin. Immunol. 106*, 228−238.

82. Beasley, C. L., and Reynolds, G. P. (1997) Parvalbumin-immunoreactive neurons are reduced in the prefrontal cortex of schizophrenics, *Schizophr. Res. 24*, 349−355.

83. Blum, B. P., and Mann, J. J. (2002) The GABAergic system in schizophrenia, *Int. J. Neuropsychopharmacol. 5*, 159−179.

84. Hashimoto, T., Volk, D. W., Eggan, S. M., Mirnics, K., Pierri, J. N., Sun, Z., and Sampson, A. R. (2003) Gene expression deficits in a subclass of GABA neurons in the prefrontal cortex of subjects with schizophrenia, *J. Neurosci. 23*, 6315−6326.